Analysis of offshore wind spectra and coherence under neutral stability condition using the two LES models PALM and SOWFA

Analysis of offshore wind spectra and coherence under neutral stability condition using the two LES models PALM and SOWFA

X Ning, M Krutova and M Bakhoday-Paskyabi
Geophysical Institute, University of Bergen and Bergen Offshore Wind Centre
E-mail: Xu.Ning@uib.no

Abstract. The Parallelized Large-Eddy Model (PALM) and the Simulator for Wind Farm Applications (SOWFA) have been used to simulate the marine boundary layer flows under neutral stability condition. The present work aims to investigate the capability of the two models in reproducing the structure of turbulence in the offshore environment through comparative analysis with a focus on wind spectra and coherence. Wind spectra obtained from the two LES solvers agree well with the empirical spectral model near the surface but show lower turbulence intensity in the low frequency range above the surface layer. Both models also produce highly consistent estimates of coherence with different horizontal and vertical separations, which match well with Davenport and IEC coherence models at height of 180m and 140m respectively. As the height decreases, LES predicts lower vertical coherence compared with the IEC model and the fitted decay coefficient for Davenport model grows as the separation distance increases.

1. Introduction

Due to the fast-growing computing power and the necessity to resolve details of flow and its interaction with offshore structures, large-eddy simulation (LES) based models have become the most eminent and powerful tools to study atmospheric boundary layer (ABL) processes for the offshore wind energy applications [1]. The Parallelized Large-Eddy Model (PALM) from Leibniz Universitat Hannover (LUH) [2] and the Simulator for Wind Farm Applications (SOWFA) [3] from the National Renewable Energy Laboratory (NREL) are two widely used codes [3, 4], but no studies have addressed comprehensive comparisons between them.

The objective of this work is to study the performance of LES solvers with different resolving strategies on modelling the coherent turbulence structures in the ABL and to observe the consistency between LES predictions and empirical formulas for wind turbulence. Such work plays an essential role in relevant wind energy applications such as wind assessment for offshore wind farms and load analysis for floating wind turbines.

In this study offshore ABL flows are simulated by two models under neutral atmospheric stability conditions. The numerical method and configuration of simulation are illustrated in section 2. We start the comparison in section 3.1 with wind shear and turbulence intensity to investigate how the two models predict the flow statistics especially in the surface layer. In section 3.2, the power spectral density of three dimension velocity fluctuations and their sensitivity to mesh resolution are then studied to reveal the energy distributions of different velocity components in two models. Finally, wind coherence derived from time series data of

two points with different horizontal and vertical separations are studied and compared with empirical coherence models in section 3.3.

2. Numerical method

2.1. Numerics and turbulence closure

SOWFA and PALM solve the filtered incompressible Navier–stokes equations with different numerical methods. The former is developed based on the pimpleFoam solver in the CFD toolbox OpenFOAM, using finite volume code for domain discretization with unstructured collocated mesh [3], while the latter employs finite element method and structured staggered mesh [2]. As for time advancement, SOWFA uses the second-order backward and PALM uses the third-order Runge–Kutta method.

Both codes ignore the density difference and introduce Boussinesq approximation to calculate the buoyancy force. SOWFA and PALM add an external source term in the momentum equation to drive the boundary layer flow and maintain the turbulence. The difference is that this driving term in PALM is assigned by a constant geostrophic wind while in SOWFA it can be set to change at every time step so that the horizontal wind speed at a certain height reaches the prescribed value. In the present study, one-equation model is used in the two codes for turbulence closure:

$$\frac{\partial e}{\partial t} + u_j \frac{\partial e}{\partial x_j} = -(\overline{u_i'' u_j''}) \frac{\partial u_i}{\partial x_j} + \frac{g}{\theta_0} \overline{u_3'' \theta''} - \frac{\partial}{\partial x_j}[-2K_m \frac{\partial e}{\partial x_j}] - \epsilon, \tag{1}$$

where the subscript $i = 1, 2, 3$ denotes the longitudinal, lateral and vertical directions respectively. g is the gravitational acceleration. t is time, x_i represents the coordinate and u_i is the filtered velocity. θ is the virtual potential temperature, with θ_0 being its value at the surface. $\overline{u_i'' u_j''}$ is the SubGrid-Scale (SGS) momentum flux and $\overline{u_3'' \theta}$ is the vertical SGS heat flux. $e = \frac{1}{2}\overline{u_i'' u_i''}$ and ϵ are SGS kinetic energy and dissipation rate respectively. The viscosity K_m is assumed to be proportion to the mixing length l and $\sqrt{e}$, and the heat diffusivity K_h is related to K_m by turbulent Prandtl number Pr_t, which is equal to 1/3 in the neutral condition [5]:

$$K_m = c_m l \sqrt{e}, \quad K_h = K_m / Pr_t, \tag{2}$$

where c_m is a model constant. According to eddy diffusivity assumption, the deviatoric SGS stress tensor and heat flux can be expressed as following:

$$\overline{u_i'' u_j''} - \frac{2}{3} e \delta_{ij} = -K_m (\frac{\partial u_i}{\partial x_j} + \frac{\partial u_j}{\partial x_i}), \tag{3}$$

$$\overline{u_i'' \theta''} = -K_h \frac{\partial \theta}{\partial x_i}. \tag{4}$$

where δ_{ij} is the Kronecker delta. A wall model based on Monin–Obukhov Similarity Theory (MOST), is introduced to estimate the momentum fluxes at the surface. A surface roughness length z_0 should be assigned for this boundary condition and in our study z_0 has values of 0.0001, 0.001 and 0.01 for different scenarios, which are typical for the sea surface [6]. Neumann and Dirichlet conditions are set to the top boundary in SOWFA and PALM respectively. The two solvers employ cyclic conditions for the vertical boundaries to develop turbulent flows and the initial velocity disturbance helps to accelerate this process.

2.2. Simulation configuration

The simulation cases for the two models use similar configurations. To assure the neutral stability condition, surface heat flux is zero and uniform temperature distribution is set from surface to 700 m height. Linearly increasing temperature with a gradient of 0.08 K/m from 700 m

to 800 m height leads to a strong capping inversion at top of the boundary layer. Coriolis force is calculated with latitude $\phi = 45°$. In SOWFA, the wind speed at height of 90 m is directly set to 8 m/s, and in PALM, several tuning simulations are necessary to find an appropriate geostrophic wind that results in the same wind profile as in SOWFA. All cases share the same computational domain with the height of 960 m and the length of 2560 m in x and y directions. The mesh resolution is the same in all three directions and various grid sizes are used to test the mesh sensitivity of two models. In order to reduce the computational cost of simulation, we exert Rayleigh damping above the height of 700 m to suppress inertial oscillations caused by Coriolis force. In this case, the horizontal velocities at various heights become stable after 20 hours simulation to reach a quasi-equilibrium state.

3. Results

In the present study, by setting the same initial and boundary conditions in SOWFA and PALM, both models generate horizontally homogeneous boundary layer flows with quite similar characteristics. No wind turbine is introduced in our simulations, but the data for computing spectra are sampled at the heights of 20 m, 100 m and 180 m, representing the typical heights of the bottom, center and top of a normal offshore wind turbine rotor.

3.1. Wind profiles

Highly consistent wind speed distributions along height from two codes are shown in Figure 1(a). As expected, the wind speed rapidly increases as leaving the surface and then increases gradually until the bottom of the inversion layer at the height of 700 m, above which a strong temperature gradient suppresses the turbulent friction and thus makes the airflow identical to the geostrophic wind. Further, according to the constant flux layer assumption and the similarity theory, the non-dimensional wind speed gradient expressed as

$$\phi_m = \frac{\kappa z}{u_*} \frac{\partial \overline{u}}{\partial z}, \tag{5}$$

where $\kappa = 0.4$ is the Von Kármán constant and u_* denotes the friction velocity, should be a constant of unity within the surface layer in neutral stability. This is correctly predicted by the two models, as seen in Figure 1(b). In a neutral atmospheric boundary layer, the airflow is dominated by a dynamic balance among geostrophic wind (pressure gradient), Coriolis force and turbulent friction. As height increases, the wind sheer becomes weak and the enhanced Coriolis force gradually rotates the flow to the direction of geostrophic wind at top of the ABL. Figure 1(c) suggests that the wind direction is rotated clockwise and the change of direction across the height range of a wind turbine rotor could reach about 4∼5 degrees. Figure 1(d) displays the vertical distributions of the turbulence intensity in three directions. The two codes have good agreement on the turbulence intensity in streamwise and vertical directions, but SOWFA predicts stronger turbulence in crosswind direction than PALM. Only the simulations with $z_0 = 0.001$ m are shown in this part and similar results are found for different surface roughness lengths.

3.2. Wind spectrum

Figure 2 displays the instantaneous contours of streamwise component of turbulent velocity at height of 100 m for SOWFA and PALM. It should be noted that in SOWFA, the main flow direction is intentionally misaligned to x-axis by 30° so that the turbulent structures are not limited around a constant position in y-direction under cyclic boundary condition. In PALM, the same problem is solved by laterally shifted the flow before it enters the inlet plane of domain.

The atmospheric boundary layer flow is characterized by randomly occurring three dimension multi-scale turbulent eddies, among which the energy transfer follows a certain rule indicated

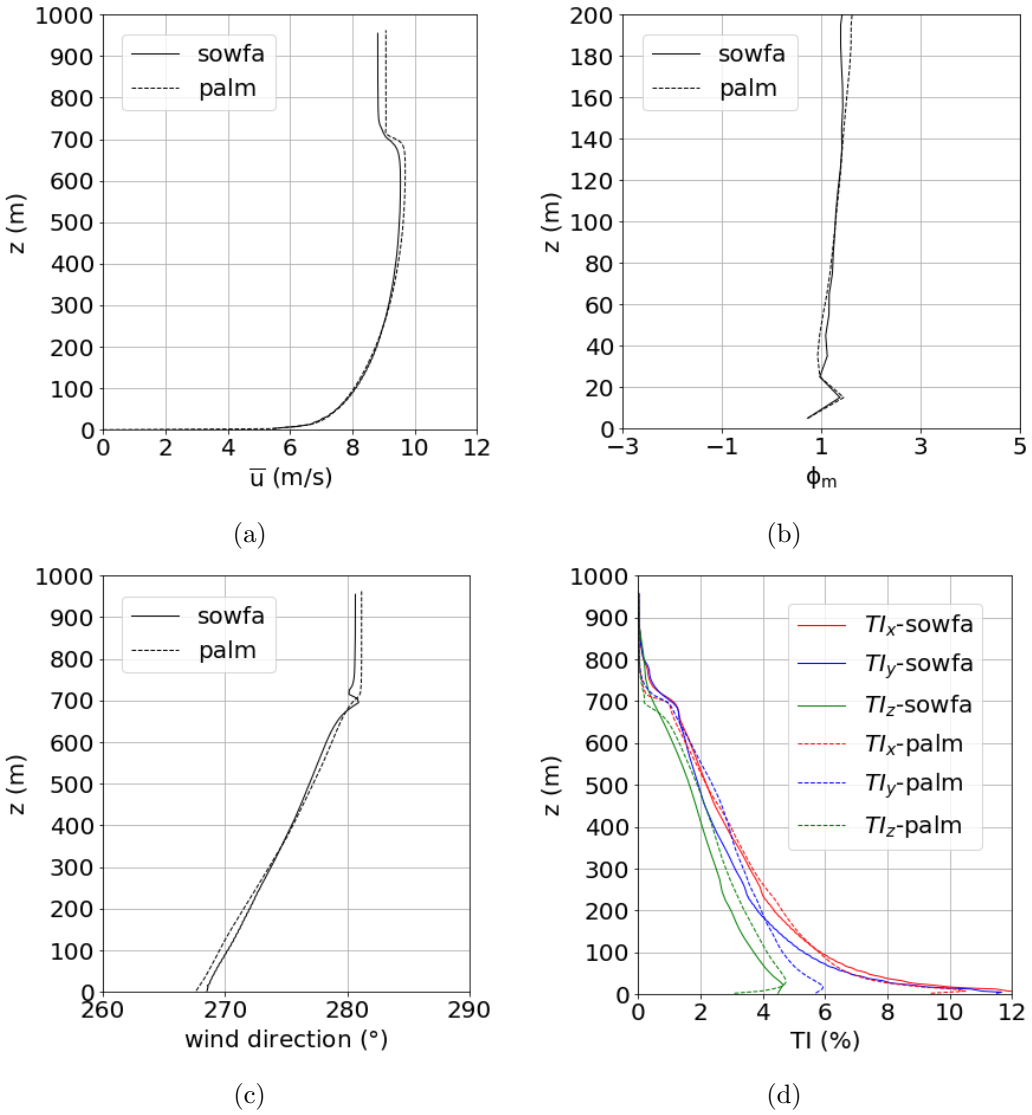

Figure 1: Profiles of wind speed (a), non-dimensional wind gradient (b), wind direction (c), three components of turbulence intensity TI_x, TI_y, TI_z (d).

by the well known K-41 theory [7]. More specifically, the wind spectrum in the so-called inertial subrange follows a $-5/3$ law. This theory is often used to examine the reality of simulations. To examine the modelling of this energy cascade, we use the 2 Hz sampled LES data at different heights and calculate the power spectral density functions averaged over various sample positions.

The wind spectra S_i $(i = u, v, w)$ derived from a large-eddy simulation can be divided into three parts: the low-frequency range where S_i has a slight negative slope or a constant value, the inertial subrange where S_i obeys the $-5/3$ power law, and the higher frequency range in which S_i drops quickly due to the cutoff effect of the LES filter. Figure 3 shows the power spectral density (PSD) of streamwise turbulent velocity at height of 100 m from simulations based on SOWFA and PALM with various grid sizes (labeled as gs). The three parts mentioned above are clearly seen in each case. Especially the cases with 5 m mesh resolution (gs5) show the longest inertial subrange for frequency between 0.02 Hz and 0.2 Hz. As the grid size increases, the

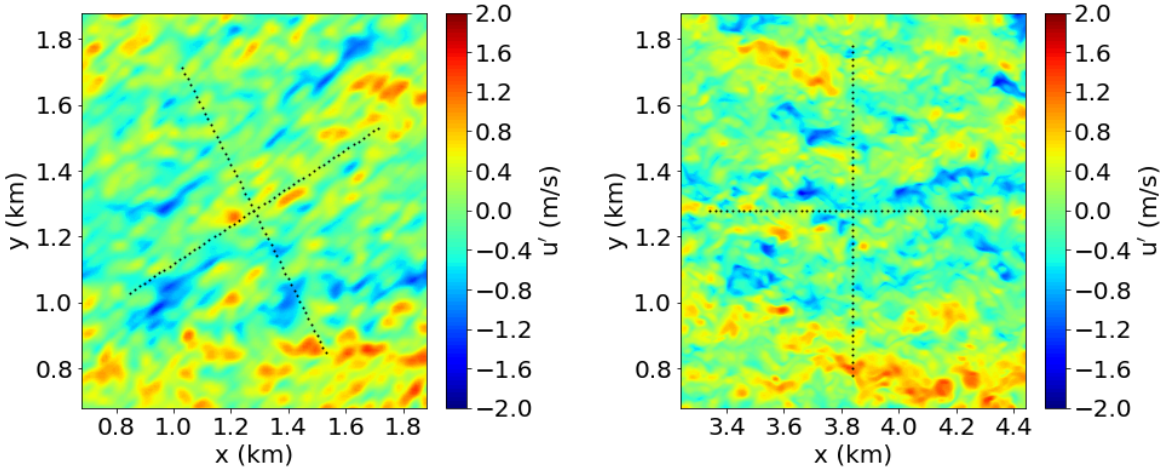

(a) SOWFA (b) PALM

Figure 2: Snapshots of u-component fluctuating velocity at height of 100 m for cases with 5 m mesh resolution and $z_0 = 0.001$ m. The black points mark the sample positions.

spectra start to drop at lower frequency but the low-frequency energy distributions of all cases demonstrate good consistency. Moreover, the profiles of Turbulence Kinetic Energy (TKE) in Figure 4 demonstrate that a mesh resolution of 5 m is fine enough for LES of a neutral boundary layer as 90% of TKE in the flow can be resolved except for the first 10m above the surface where the turbulence is parameterized by the wall model.

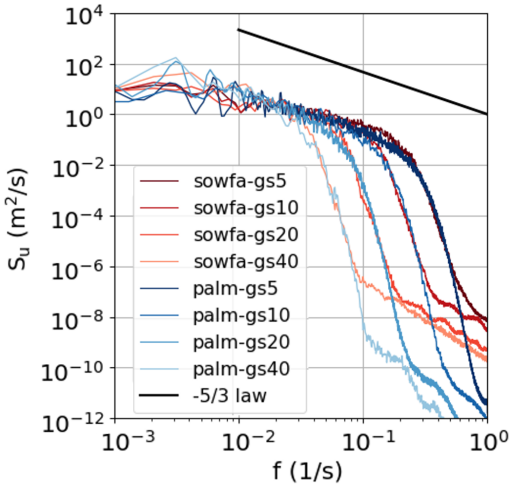

Figure 3: Power spectral density curves of u-component fluctuating velocity at height of 100 m for cases with various mesh resolutions and $z_0 = 0.001$ m.

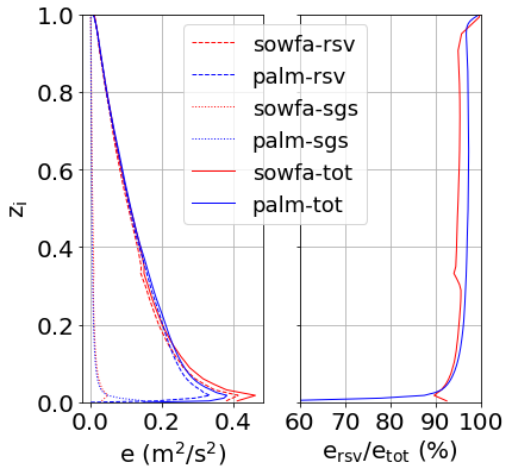

Figure 4: Profiles of TKE for cases with 5 m mesh resolution. z_i denotes the height normalized by the boundary layer height. e_{sgs}, e_{rsv} and e_{tot} represent the subgrid-scale, resolved-scale, and total TKE respectively.

Figure 5 further shows the scaled power spectral density fS_i/u_*^2 at three heights for simulations with different surface roughness lengths and Kaimal spectral model [8] is also plotted

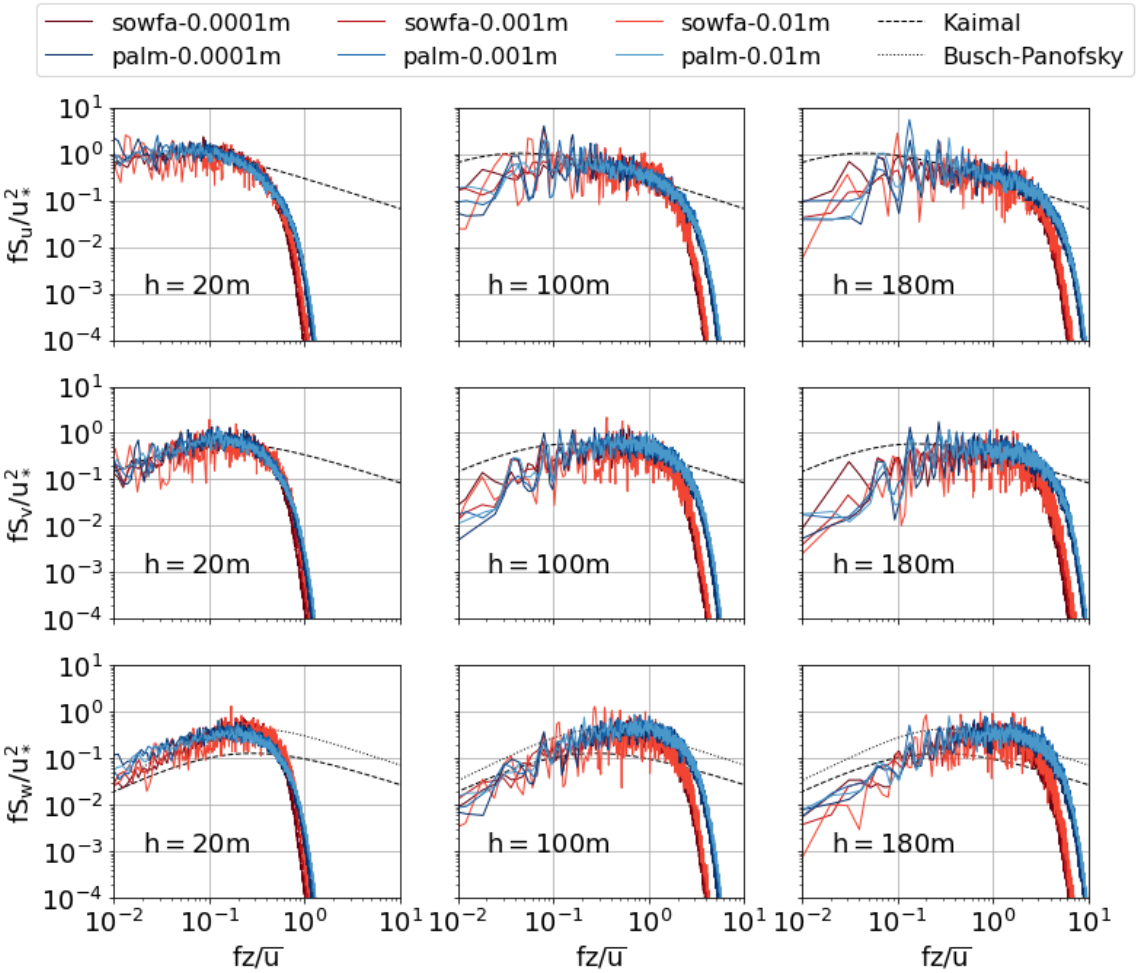

Figure 5: Scaled power spectral density of turbulent velocities in three directions at heights of 20 m, 100 m, 180 m.

as a reference. At height of 20 m, the spectra of velocities in all directions for both models perfectly collapse and the normalized spectra for cases with different surface roughness lengths follow the same curve. At heights of 100 m and 180 m, SOWFA and PALM still have good agreements at low-frequency and inertial subrange, but turbulence in PALM contains more energy than in SOWFA at the dropoff frequency range. In addition, it is found that given the same height above surface layer, the normalized PSD increases with increasing surface roughness length.

Furthermore, the spectra of horizontal velocity components at height of 20 m follow exactly the Kaimal spectra, indicating an accurate reproducion of the shear turbulence within the surface layer. However, at higher height levels, both LES models predict lower PSD values at low-frequency range and this deviation becomes larger as height increases. The underestimation of the energy of large-scale turbulence above the surface layer could partly be attributed to the limited size of simulation domain, and more importantly, this also implies the necessity of the coupling with meso-scale model in order to simulate turbulence structures with size of several kilometers. For w-component, spectra from LES have larger energy level than the Kaimal spectra. However, it is found that the spectral model for w-component proposed by Busch and Panofsky [9] (shown in the last row of Figure 5) matches better the simulation results.

3.3. Coherence

Wind spectrum reveals energy distribution in turbulent flows, but it contains no information of their coherent structures. Therefore we discuss the wind coherence in this section to study the correlation of velocity fluctuations in different spatial positions. Co-coherence, quad-coherence and root-coherence are defined as the real part, imaginary part and amplitude of two-point cross-spectrum normalized by the product of power spectra for each point respectively i.e.,

$$\begin{aligned} co\text{–}coh(f) &= \frac{\mathrm{Re}[S_{xy}(f)]}{\sqrt{S_{xx}(f)S_{yy}(f)}}, \quad quad\text{–}coh(f) = \frac{\mathrm{Im}[S_{xy}(f)]}{\sqrt{S_{xx}(f)S_{yy}(f)}}, \\ coh(f) &= \sqrt{co\text{–}coh^2(f) + quad\text{–}coh^2(f)}, \quad (S_x(f),\ S_y(f) \neq 0). \end{aligned} \tag{6}$$

By definition, the coherence varies between 0 and 1. A large value of $coh(f)$ indicates the two positions are highly correlated by the same eddy at frequency of f. Such coherent turbulence will exert unevenly distributed inflow on a wind turbine and increase the structural loads, especially for those with large rotor size and floating foundation in offshore environment [10, 11]. Coherence could exist among all components of the velocity, but previous researches demonstrate that wind turbine loads are more sensitive to the coherence of fluctuations in primary wind direction with lateral and vertical separations [12, 13], which are thus the main focus of the present study.

It should be noted that if the time series are directly used without any smoothing or averaging, the resulting estimates of coherence will be equal to unity at all frequencies [14]. To avoid this problem, the sampled time series are split into several subsegments with 50% overlapping and the derived power spectral and cross spectral density are then averaged to obtain the final coherence function computed by Eq. (6). However, statistical errors are still inevitable because of the finite data sampling time length T_s and sampling frequency f_s. The length of each subsegment L_s also affects the quality of estimates. These parameters should be carefully selected to reduce the uncertainty of our results as much as possible meanwhile keep the computational cost in an acceptable level. Therefore, we firstly analyze the sensitivity of estimated co-coherence to these processing parameters in order to find an appropriate way to achieve reliable results.

Figure 6 displays the sensitivity of the estimated co-coherence of 40 m lateral separation to sampling time T_s, sampling frequency f_s and subsegment length L_s. We use $T_s = 2400$ s, $L_s = 240$ s and $f_s = 2$ Hz as a reference value set and for each plot only one of the three parameters is changed to investigate its effects. The results of every sample point pair are averaged to further reduce errors and the resulting standard deviation becomes a qualitative description of the uncertainty level of estimation. Figure 6(a) illustrates that given the same f_s and L_s, sampled data with various time lengths provide co-coherence results of good convergence. It is also clearly shown that the standard deviation decreases as the sampling time increases. This indicates that lengthening the sampling time will effectively reduce the uncertainty of estimates. The simulation shows that wind coherence disappears rapidly when the frequency increases, which has clear physical meaning that small turbulent eddies cannot maintain their coherence in a long distance. The frequency range of concern for coherence is from 0 Hz to about 0.1 Hz. Figure 6(b) shows that a sampling frequency of 2 Hz is enough and further increasing f_s will not reduce uncertainty but consume more computation and storage resource.

Figure 6(c) illustrates the effects of subsegment length with fixed sampling time and frequency. A longer L_s means more data points are used to derive spectra within the frequency range of concern, giving higher spectra resolution, but a longer subsegment (smaller number of subsegments) will also increase the statistical errors and thus reduce the reliability of estimation. In our case, a subsegment length less than 120 s leads to large distortion in the low frequency range, while results for $L_s = 480$ s seem to strongly vary among different sample point pairs. Based on the above analysis, we use $T_s = 7200$ s, $f_s = 2$ Hz and $L_s = 240$ s for the computation of coherence in the following discussions.

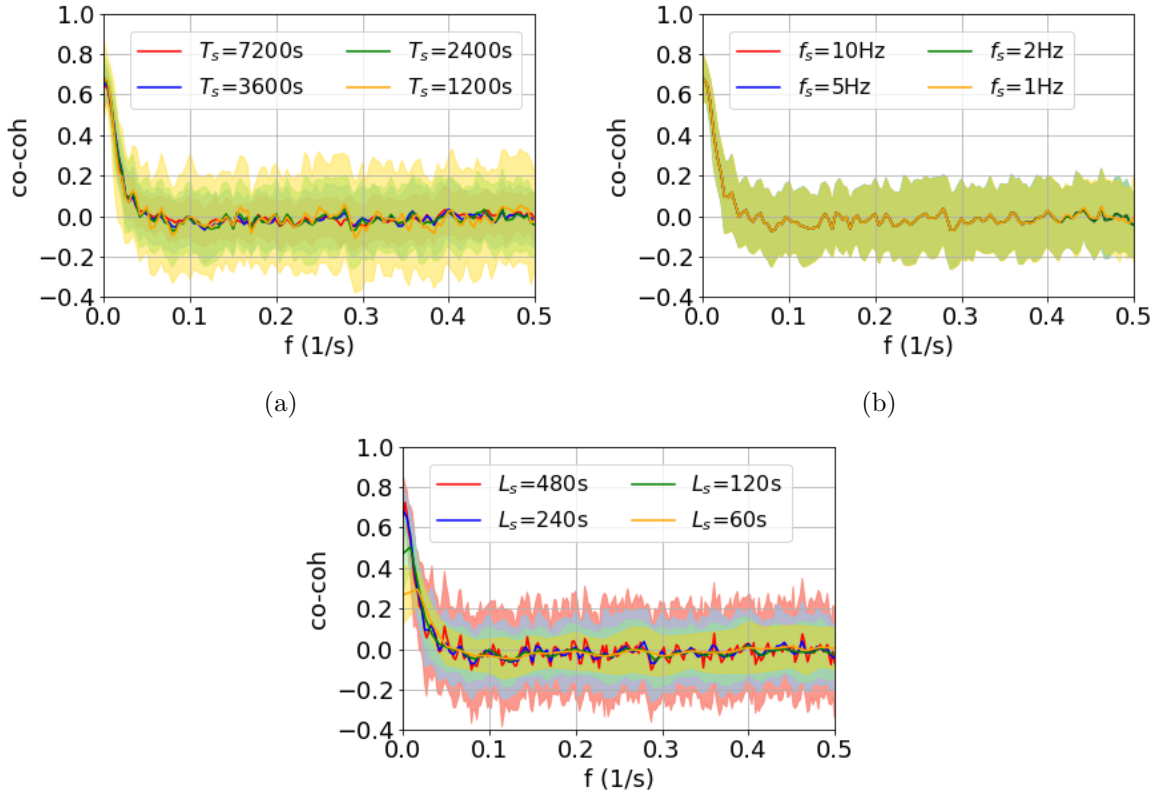

Figure 6: Sensitivity of estimated co-coherence to sampling time T_s (a), sampling frequency f_s (b) and subsegment length L_s (c).

The estimated lateral coherence of alongwind component at heights of 20 m, 100 m and 180 m from the two LES models are displayed in Figure 7. The two LES models provide highly consistent coherence results especially at heights of more than 100 m. As expected, strong lateral coherence exists for separation up to 80 m and decreases rapidly with frequency and separation distance. This can be further described quantitatively by fitting the Davenport coherence model [15], which assumes the coherence decays as an exponential function of reduced frequency $f\delta/\overline{u}$, to the LES data:

$$coh_{\mathrm{D}}(f,\delta,\overline{u}) = \exp\left(-a\frac{f\delta}{\overline{u}}\right), \tag{7}$$

where δ and $\overline{u}$ represent the separation distance and mean wind speed at the corresponding height. The decay coefficient a is used as the fitting parameter. At height of 180 m, the fitted model curves for different separations overlap each other with close decay coefficients, showing that this similarity is well described by the reduced frequency. The data at 100 m height also follow the exponential decay well, but the decay coefficient obviously increases with increasing separation distance. This is partly due to the fact that the coherence of large separation at low height levels is not unity at zero frequency [14], resulting in a larger fitted decay coefficient.

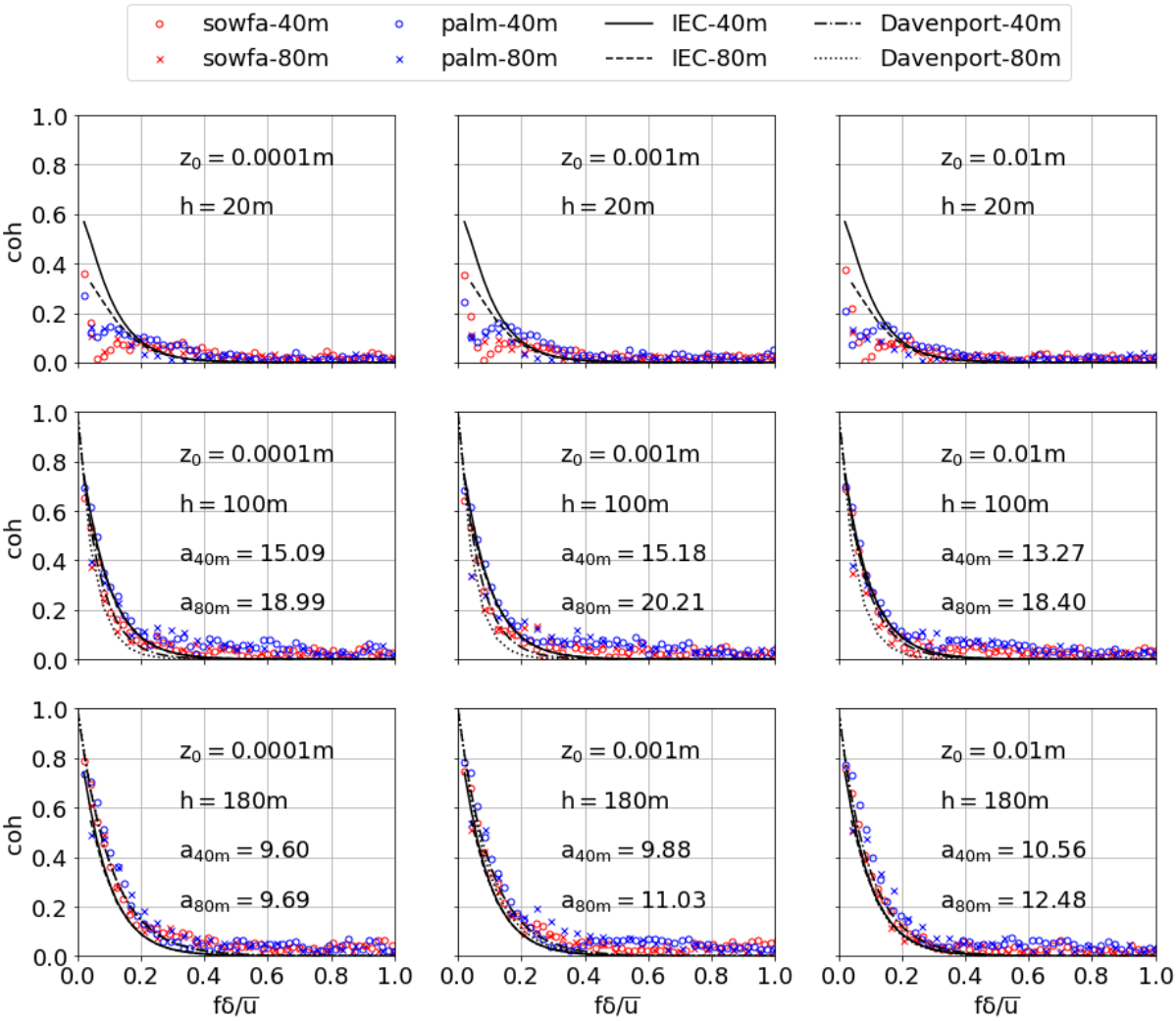

Figure 7: Estimates of lateral coherence based on LES data along with Davenport and IEC coherence models.

Based on Davenport model, the IEC coherence model [16]

$$coh_{\mathrm{IEC}}(f,\delta,\overline{u}) = \exp\left(-12\sqrt{\left(\frac{f\delta}{\overline{u}}\right)^2 + \left(\frac{0.12\delta}{8.1L}\right)^2}\right), \quad L = \begin{cases} 0.7z & \text{if } z < 60m \\ 42m & \text{if } z \geq 60m \end{cases}, \tag{8}$$

adds a length scale parameter L to account for this problem. It has been widely used to describe the turbulence coherence for the design of offshore structures and our results from the two LES models have better agreement with the IEC model at height of 100 m. It should be noted that the coherence spectra at height of 20 m from LES have much smaller values due to the blocking effect of the ground and do not follow well the IEC model. Similar results can be found in a relevant study of lidar measurements [17].

Figure 8 shows the estimates of vertical coherence from LES, accompanied with fitting curves of Davenport model and also the IEC model, expressed as functions of reduced frequency. Here the heights of concern are changed to 60 m and 140 m because these heights correspond to the middle heights of the upper and lower parts of a rotor, where the vertical turbulent flow

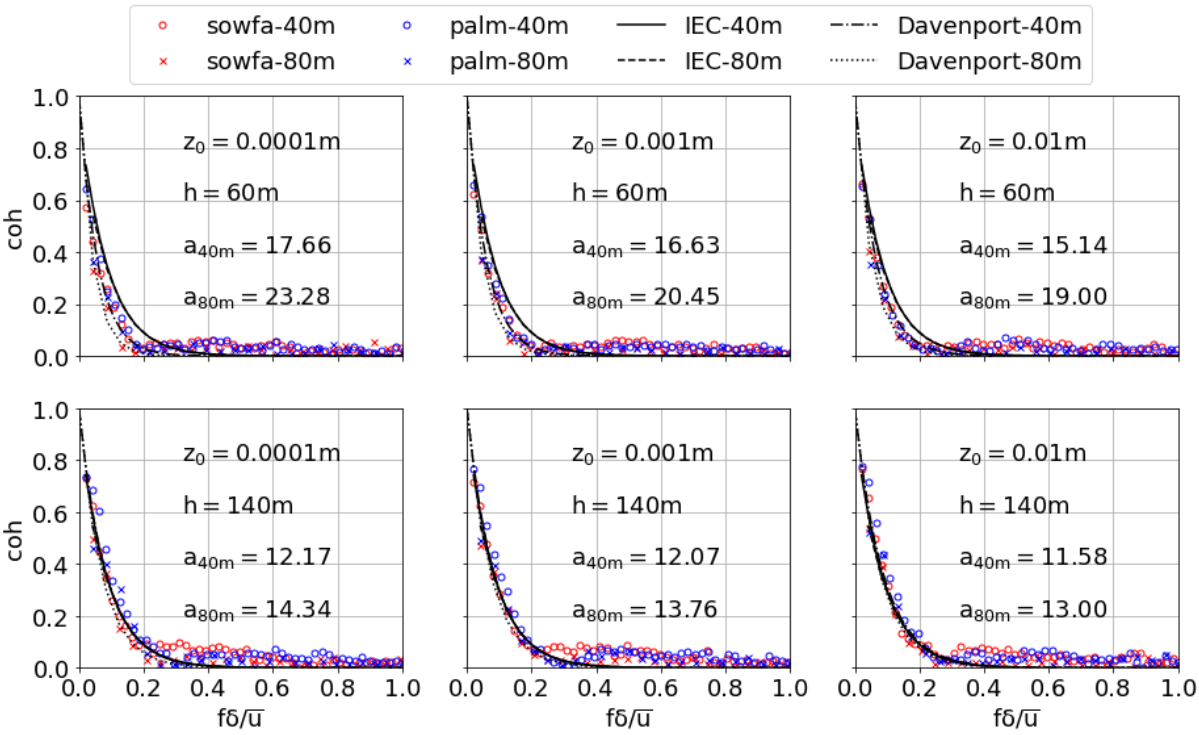

Figure 8: Estimates of vertical coherence based on LES data along with Davenport and IEC coherence models.

contributes the most to the structural loads of a wind turbine. We observe perfect agreements among LES results, Davenport model, and IEC coherence model at height of 140 m. Meanwhile this figure also shows that the estimates of vertical coherence for 40 m and 80 m separations follow nearly the same curve though the decay coefficient for larger separation has a slightly larger value. However, the two LES models show lower vertical coherence compared with the IEC model at height of 60 m and a larger separation leads to faster decay of coherence with increasing reduced frequency as shown by fitted Davenport model curves. Moreover, LES results show that the increasing surface roughness could lead to larger vertical coherence at a given height, but this effect is small.

4. Conclusions

We employed two numerical models (SOWFA and PALM) to implement large-eddy simulations (LES) of neutral atmospheric boundary layer flows over typical surface roughness lengths for ocean surface. The static and dynamic features of simulated wind fields were illustrated and analysed through wind profiles, power spectra and coherence.

The two models provided nearly identical profiles of wind speed, direction and turbulence intensity across the boundary layers in all scenarios, demonstrating their good capture of the turbulent friction and the effect of Coriolis force. A mesh resolution of 5 m was found to be fine enough to resolve 90% of the turbulence kinetic energy. The two LES models provided wind spectra in agreement with the empirical spectral models near the surface but showed lower energy of large-scale turbulence above the surface layer compared to the empirical models.

The sampling time, frequency and the subsegment length are carefully chosen based on sensitivity analysis to minimize the errors in data processing for coherence estimation. The coherence results from simulations showed high consistency between the two LES models.

Furthermore, we showed that at relatively high heights LES agreed well with both the IEC coherence model and the Davenport model and the curves for different separations overlapped each other, while at lower heights (below 100 m) the IEC coherence model showed better agreement with LES than the Davenport model for lateral coherence but gave higher estimation than LES for vertical coherence.

5. Acknowledgements

This work is part of the LES-WIND project and the authors would like to acknowledge the funding from the academic agreement between University of Bergen and Equinor. The simulations were performed on resources provided by UNINETT Sigma2 - the National Infrastructure for High Performance Computing and Data Storage in Norway.

References

[1] Stoll R, Gibbs J A, Salesky S T, Anderson W and Calaf M 2020 *Boundary-Layer Meteorology* **177(2)** 541–581
[2] Maronga B *et al* 2020 *Geoscientific Model Development* **13(3)** 1335–1372
[3] Churchfield M J, Lee S, Michalakes J and Moriarty P J 2012 *Journal of turbulence* **1(13)** N14
[4] Vollmer L, Steinfeld G, Heinemann D and Kühn M 2016 *Wind Energy Science* **1(2)** 129–141
[5] Deardorff J W 1972 *Journal of Atmospheric Sciences* **29(1)** 91–115
[6] Golbazi M and Archer C L 2019 *Advances in Meteorology* **2019** 5695481
[7] Kolmogorov A N 1941 *Cr Acad. Sci. URSS* **30** 301–305
[8] Kaimal J C, Wyngaard J C, Izumi Y and Coté O R 1972 *Quarterly Journal of the Royal Meteorological Society* **98(417)** 563–389
[9] Busch N E and Panofsky H A 1968 *Quarterly Journal of the Royal Meteorological Society* **94(400)** 132–148
[10] Eliassen L, Jakobsen J and Krokstad J 2015 *14th Int. Conf. on Wind Engineering* Porto Alegre, Brazil 2015
[11] Anderson O J and Løvseth J 2006 *Marine Structures* **19(2-3)** 173–192
[12] Robertson A N, Shaler K, Sethuraman L and Jonkman J 2019 *Wind Energy Science* **4(3)** 479–513
[13] Doubrawa P, Churchfield M J, Godvik M and Sirnivas S 2019 *Applied Energy* **242** 1588–1599
[14] Kristensen L and Jensen N O 1979 *Boundary-Layer Meteorology* **17(3)** 353–373
[15] Davenport A G 1961 *Quarterly Journal of the Royal Meteorological Society* **87(372)** 194–211
[16] International Electrotechnical Commission 2006 *IEC 61400–1 Wind Turbines-Part 1: Design requirements*
[17] Cheynet E, Jakobsen J B, Svardal B, Reuder J and Kumer V 2016 *Energy Procedia* **94** 462–477